

Magnon polaron formed by selectively coupled magnon and phonon modes in a ferromagnetic nanograting

Felix Godejohann^{1*}, Alexey V. Scherbakov^{1,2*}, Serhii M. Kukhtaruk^{1,3}, Alexander N. Poddubny², Dmytro D. Yaremkevich¹, Mu Wang⁴, Achim Nadzeyka⁵, Dmitri R. Yakovlev^{1,2}, Andrew W. Rushforth⁴, Andrey V. Akimov⁴, and Manfred Bayer^{1,2}

¹Experimentelle Physik 2, Technische Universität Dortmund, Otto-Hahn-Str. 4a, 44227 Dortmund, Germany.

²Ioffe Institute, Polytechnicheskaya 26, 194021 St. Petersburg, Russia.

³Department of Theoretical Physics, V.E. Lashkaryov Institute of Semiconductor Physics, Pr. Nauky 41, 03028 Kyiv, Ukraine.

⁴School of Physics and Astronomy, University of Nottingham, Nottingham NG7 2RD, United Kingdom.

⁵Raith GmbH, Konrad-Adenauer-Allee 8, 44263 Dortmund, Germany

*e-mail: felix.godejohann@tu-dortmund.de; alexey.shcherbakov@tu-dortmund.de.

A magnon polaron is the hybridized state of strongly coupled phonon and magnon, the elementary quanta of lattice vibrations and spin waves in a magnetically-ordered material. Magnon polarons form at the intersection of magnon and phonon dispersions. Their observation in the time domain has remained extremely challenging, because the weak interaction of magnons and phonons and their short lifetimes jeopardize the strong coupling required for hybridization. Here, we overcome these limitations by accurate spatial matching of the magnon and phonon waves in a nanograting fabricated from a metallic ferromagnet. The spatial overlap of the selected phonon and magnon modes results in a high coupling strength, which in combination with long lifetimes allows us to find clear evidence of highly-cooperative magnon-phonon hybridization.

INTRODUCTION

Magnons are the collective spin excitations in magnetically-ordered materials. Nowadays the coherent manipulation of high-frequency magnons on the nanoscale is one of the most prospective concepts for information technologies, also in the quantum regime. In this respect, the hybridization of magnons with phonons has been considered as a powerful tool for spin control [1-7]. Magnon-phonon hybridization in bulk materials is well understood theoretically [8,9] and has been realized experimentally in the MHz frequency range [10]. However, on the nanoscale, where magnon and phonon frequencies reach the GHz and sub-THz frequency ranges, magnon-phonon hybridized states, in the following referred to as magnon polarons, are not yet understood or utilized.

Direct evidence of the formation of magnon polarons would be the avoided crossing of the magnon and phonon dispersion curves at their intersection [8,9]. A spectral gap between the two branches arising from hybridization clearly indicates strong coupling of two underlying excitations, like in the case of two strongly coupled harmonic oscillators [11]. The experimental observation of the avoided crossing for magnon polarons is possible when the energy splitting at magnon-phonon resonance exceeds the spectral widths of the interacting modes. Quantitatively, the hybridization is characterized by the cooperativity $C = \kappa^2 / \gamma_{\text{ph}} \gamma_{\text{M}}$, where κ is the coupling strength, i.e. the energy exchange rate between phonons and magnons, and γ_{ph} and γ_{M} are their individual damping rates. High cooperativity $C \gg 1$ ensures deterministic manipulation of the coupled states with periodic conversion of magnons into phonons and vice versa with high fidelity, but is extremely challenging to realize in practice due to the weak magnon-phonon interaction and their short lifetimes.

Here, we demonstrate an original approach for achieving hybridization of magnons and phonons with high cooperativity in a metallic ferromagnet. By spatial patterning of a ferromagnetic film into a nanograting (NG), we achieve magnon and phonon modes with significantly long lifetimes. By

spatially matching of their wave distributions we select particular modes in the phonon and magnon spectra for hybridization. This allows us to solve the main problem preventing strong magnon-phonon coupling in ferromagnetic metals, namely quick dephasing of the interacting excitations, and we achieve $C \approx 8$ sufficient for pronounced magnon polaron formation. The suggested approach is verified in time-resolved experiments revealing the avoided crossing between the magnetic polaron branches in the transient magnon evolution that is excited by a femtosecond optical pulse. We demonstrate and discuss the scenarios in which coherent magnon polarons are generated and detected depending on the spatial symmetry of the phonons and magnons in the nanostructure and on the initial and boundary conditions of the coupled system. Our theoretical analysis based on coupled oscillators illustrates the physics behind the experimental observations.

RESULTS

Galfenol nanograting and experimental technique

In the experiments, we use the magnetostrictive alloy of iron and gallium, known as Galfenol ($\text{Fe}_{0.81}\text{Ga}_{0.19}$), grown on a GaAs substrate. This metal possesses strong magnon-phonon interaction [12] and pronounced magnon resonances [13,14]. Lateral nanoscale patterning is used to obtain a NG of shallow parallel grooves with a total lateral size of $25 \times 25 \mu\text{m}^2$, illustrated in Fig. 1A. The experimental technique is shown in the bottom panel of Fig. 1A and is based on conventional magneto-optical pump-probe spectroscopy (see the Materials and Methods section for details). The pump pulse of 150-fs duration, and excitation energy density of 12 mJ/cm^2 , focused to a spot of 10-microns diameter, excites coherent responses of the lattice and magnetization. The linearly polarized probe pulse focused to a spot of 1-micron diameter at the NG front side in the center of the pump spot is used for monitoring the phonon and magnon dynamics. By measuring the intensity of the reflected probe pulse, $\Delta I(t)$, where t is the time delay between probe and pump, we monitor the coherent phonon response of the NG [15]. To measure the time evolution of the magnetization, we use a detection scheme that monitors the polar Kerr rotation (KR) of the probe's polarization plane, $\Psi(t)$ [16]. An external magnetic field, B , applied in the NG plane is used to adjust the magnon spectrum.

Localized phonon modes in the nanograting

The phonon spectrum generated by the pump pulse comprises several phonon modes localized in the near-surface region of the NG. These modes are excited due to the strong absorption (20-nm penetration depth) of the pump pulse in Galfenol. The calculated spatial profiles of the atom displacements of these localized modes are shown in Fig. 1B. Both modes are standing pseudo-surface acoustic waves [17], which possess two displacement components along the x - and z -axes. Therefore, they are characterized by three components of the dynamical strain tensor: η_{xx} , η_{zz} , η_{xz} , the frequencies and phases of which remain preserved within the phonon mode lifetimes. The mode shown in the lower panel of Fig. 1B is a Rayleigh-like standing wave with dominant displacement along the z -axis, i.e. perpendicular to the NG plane. We refer to this mode as the quasi-transverse acoustic (QTA) mode. It is important to mention that there is an antisymmetric counterpart of the QTA mode, which cannot be excited optically. This localized mode is almost degenerate with the QTA mode, but as shown below, plays a crucial role in the interactions with magnons.

Another mode, shown in the top panel of Fig. 1B is often referred to as a surface skimmed longitudinal mode [18]. It has a predominant in-plane displacement and we refer to it as the quasi-longitudinal acoustic (QLA) mode. The calculated frequencies of the QTA and QLA modes are 13.1 and 15.3 GHz, respectively, and they both can be excited with similar expected amplitudes and lifetimes. However, due to its specific polarization and spatial distribution, the QLA mode provides a much smaller contribution to the reflectivity signal (see the Materials and Methods section for

details). This can be seen in $\Delta I(t)$ and the corresponding fast Fourier transform (FFT) shown in Fig. 1C, where the lower-lying spectral line at $f_{\text{QTA}}=13.0$ GHz has a large amplitude, while the upper QLA mode is invisible. The lifetime of the QTA mode, obtained from the decay of the transient reflectivity signal, is 5.3 ns, which agrees with the half width at half maximum (HWHM) $\gamma_{\text{QTA}}=0.03$ GHz in the associated power density spectrum (for details of the measurements, the fitting procedure and the relation between the modes' lifetimes and their FFT spectral widths see the Materials and Methods section). The Q -factor of the QTA phonon mode therefore exceeds 200.

Magnon modes in the nanograting and the experimental concept

Because the studied grating contains shallow grooves, the depths of which are much smaller than the NG period and the ferromagnetic film thickness, the magnon spectrum is close to that of an unpatterned film [19]. The transient KR signal measured for a plain Galfenol film (outside the NG) is shown in Fig. 1D. The oscillations reflect the magnetization precession excited by the femtosecond optical pulse, which induces ultrafast changes of the magnetic anisotropy [20,21]. The magnon spectrum of the plain film consists of several magnon modes quantized along the z -axis [14,20]. At $t > 1$ ns the fundamental magnon (FM) mode with the lowest frequency $f_{\text{FM}}=18.2$ GHz at $B=200$ mT contributes solely to the KR signal. In the whole range of magnetic fields used in the experiment, it has a considerably long lifetime $\tau_{\text{FM}}=0.95$ ns with the respective HWHM in the power density spectrum $\gamma_{\text{FM}}=0.17$ GHz. In the NG, the magnon modes undergo additional spatial modulation along the x -axis with the NG period d due to the periodically modulated demagnetizing field (shape anisotropy) [19]. Despite this modulation, the FM mode remains the most pronounced in the NG magnon spectrum and possesses the same spectral width and a similar dependence of frequency on B as in the plain Galfenol film [19]. The main object of our study is the interaction of this FM mode with the two localized phonon modes, QTA and QLA.

The idea of our experiment is demonstrated schematically in Fig. 1E, showing the predicted magnetic field dependences of the frequencies for the uncoupled phonon and FM modes. For the phonons, the frequencies are independent of B as shown by the horizontal lines. For the FM mode, the B -dependence is linear in the magnetic field range of interest. Magnon-phonon hybridization is expected at the crossing points. Experimentally, we measure the transient KR signals while varying B to tune the magnon frequency. Through the FFTs of the transient signals, we obtain information about the FM spectrum paying special attention to the resonance conditions.

Avoided crossing at the magnon-phonon resonance

Figure 2 summarizes our main experimental observations. The color contour map in Fig. 2A shows the field dependence of the spectral amplitude density of the transient KR signal. The pivotal result is the well-resolved avoided crossing observed at the magnon-phonon resonance located at $B=110$ mT. The normal mode splitting at the nominal intersection of the FM and QTA modes, Δ , obtained by a fit to the transient KR signal and from its FFT, is quantified as $\Delta = 0.4$ GHz. The presence of the avoided crossing and the value of Δ are demonstrated also in Fig. 2B, which shows the field dependence of the frequencies of the two spectral peaks in the measured FFT spectra around 13.0 GHz. Figure 2C shows the transient KR signals and their spectra obtained for off-resonant ($B=30$ mT) and resonant ($B=110$ mT) conditions. For off-resonance the spectrum consists of a broad magnon band including a peak at f_{FM} , that corresponds to the FM mode, and two intense narrow peaks at the frequencies of the QTA and QLA phonon modes. Their existence in combination with high amplitudes is due to the driving of higher-order magnon modes in the NG by the localized QTA and QLA phonon modes [22]. For on-resonance when the frequency of the FM mode, f_{FM} , coincides with the frequency of the QTA phonon mode, f_{QTA} , the normal mode splitting around $f=f_{\text{FM}}=f_{\text{QTA}}$ is observed (see also the

zoomed section in Fig. 2D), which uniquely indicates the avoided crossing. This gives direct evidence of the magnon polaron, i.e. the optically excited, hybridized magnon-phonon state.

The resonance of the FM mode with the QLA mode is evidently seen as the bright red spot in Fig. 2A at $B=140$ mT when $f_{\text{FM}}=f_{\text{QLA}}$. The transient KR signals and spectra measured at this resonance are shown in Fig. 3A. The strong increase of the spectral amplitude at the QLA mode frequency, whose field dependence is shown in the left panel of Fig. 3B is the result of resonant phonon driving of magnetization precession [7,18,22-25], which clearly indicates magnon-phonon interaction. However, no avoided crossing is observed for the FM-QLA resonance.

Summarizing the main experimental results, we clearly observe magnon polaron formation for the FM-QTA resonance through the normal mode splitting, but no avoided crossing is detected for the FM-QLA resonance. Another important difference between the two resonances is the strong increase of the KR signal due to phonon driving, which is observed only for the FM-QLA resonance.

Symmetries of the modes and their selective coupling

To understand the different manifestations of the magnon-phonon interaction in the NG at the two resonances, we analyze this interaction in more detail. Our analysis is based on the approach developed in Ref. [26]. There it was shown that the coupling strength of interacting magnon and phonon modes is determined by the spatial overlap of the dynamical magnetization, $\delta\mathbf{m}$, of a magnon mode with the strain components of a phonon mode. The interacting magnon and phonon modes can be considered as two coupled oscillators [26]. Due to the in-plane orientation of the external magnetic field, the z -component of the steady-state magnetization can be assumed to be zero. In this case, for modeling the magnon-phonon interaction we have to consider only two strain components: η_{xx} and η_{xz} [22]. The coupling strength, $\kappa \approx \Delta/2$ of the magnon and phonon modes at resonance is defined by two overlap integrals:

$$\kappa = \beta_1 \int \tilde{\eta}_{xx} \delta\tilde{m}_x dV + \beta_2 \int \tilde{\eta}_{xz} \delta\tilde{m}_z dV, \quad (1)$$

where $\delta\tilde{m}_{x,z}$ and $\tilde{\eta}_{xx,xz}$ are the components of the dynamical magnetization of the magnon mode and of the strain components of the phonon mode, respectively, normalized in such a way that $\int \delta\tilde{m}_{x,z}^2 dV = \int \tilde{\eta}_{xx,xz}^2 dV = 1$ (dV is a dimensionless unit volume element). The coefficients β_1 and β_2 , which have the dimension of frequency, are defined by the material parameters including the magneto-elastic coefficients, the saturation magnetization M_s , the mass density of the media, as well as the external magnetic field orientation and the resonance frequency [10].

To evaluate Eq. (1) we consider the spatial distributions of the phonon modes localized in the NG. As mentioned earlier, there is a counterpart of the QTA mode referred to as QTA*. The spatial distributions of their strain components are shown in the bottom of Fig. 4A. The QTA and QTA* modes split due to Bragg reflections and interferences in the spatially periodic NG [27], but their splitting does not exceed 0.1 GHz. Thus, the QTA and QTA* modes may be considered as degenerate. The calculated HWHM of both modes, which is determined by escape to the substrate, is much smaller than the measured value of 0.03 GHz for the QTA mode, so that the width is determined by NG imperfections. Thus, we may assume $\gamma_{\text{QTA}^*}=\gamma_{\text{QTA}}$. The only difference between the QTA and QTA* modes is the symmetry along the x -axis. We call the QTA mode *symmetric* due to the symmetry of the strain components $\tilde{\eta}_{xx}$ and $\tilde{\eta}_{zz}$ relative to the center of the NG groove. The QTA* mode is called accordingly *antisymmetric*. The optical activity of the QTA and QTA* phonon modes is determined by the spatial overlap with the light field of the pump and probe pulses inside the NG, which has a symmetric distribution. Thus, only the symmetric QTA mode is excited by the pump and detected in the transient intensity signal. The QTA* mode can be neither excited by the pump nor optically detected due to the antisymmetric profile of $\tilde{\eta}_{zz}$. However, the shear strain component $\tilde{\eta}_{xz}$, which

contributes to the interaction with magnons, has the opposite symmetry: it is antisymmetric for QTA and symmetric for QTA* (see Fig. 4a).

Next, we consider the magnon spatial distribution, assuming mixed boundary conditions for the magnetization along the z-axis: pinning at the (Fe,Ga)/GaAs interface and free precession at the patterned surface of the NG. Our choice is based on Ref. [14], which reports pinning boundary conditions for both interfaces of a plain Galfenol film grown on a GaAs substrate and covered by an antiferromagnetic Cr layer. However, it is reasonable to suggest that in a patterned structure with the Cr-cap removed (within and around the grooves), the open surface is characterized by the free boundary condition for the precessing magnetization. Then, the spatial distribution of the normalized dynamic magnetization, $\widetilde{\delta\mathbf{m}}$, for the FM mode can be written as

$$\widetilde{\delta m_x} = \widetilde{\delta m_z} = A \cos\left(\frac{2\pi}{d}x\right) \sin\left(\frac{\pi}{2h}z\right), \quad (2)$$

where $z=0$ corresponds to the (Fe,Ga)/GaAs interface. The spatial distribution of $\widetilde{\delta\mathbf{m}}$ is shown in the center of Fig. 4A.

Calculations based on Eqs. (1) and (2) show that the coupling strength of the FM mode with the QTA* mode is three orders of magnitude stronger than with the QTA mode in the NG. This selectivity is provided by the ideal spatial matching of $\widetilde{\delta\mathbf{m}}$ and the shear strain component $\widetilde{\eta}_{xz}$ of the QTA* mode, while the poor matching of the FM mode and the QTA phonon mode fully suppresses their interaction. Therefore, we conclude that the experimentally observed hybridization corresponds to the coupling of the FM with the antisymmetric QTA* mode. The QTA* phonon mode is not excited optically and, therefore, driving of the FM mode by QTA* does not take place. This explains the experimental observation of the avoided crossing effect without resonant driving by phonons, as demonstrated in Fig. 2.

Cooperativity of the magnon-phonon coupling and model of coupled oscillators.

The value of the measured spectral splitting $\Delta = 0.4$ GHz ($\kappa_{\text{QTA}^*} = 0.2$ GHz) at resonance and the known values of $\gamma_{\text{FM}}=0.17$ GHz, $\gamma_{\text{QTA}^*}=0.03$ GHz allow us to estimate the cooperativity of the magnon-phonon coupling at the intersection of the FM and QTA* modes: $C_{\text{QTA}^*} = \kappa_{\text{QTA}^*}^2 / (\gamma_{\text{QTA}^*} \gamma_{\text{FM}}) = 7.8$. This value exceeds $C = 1$ by almost an order of magnitude, ensuring the strong coupling regime and the hybridization of magnons and phonons for on-resonance conditions. This is confirmed by the spectral width of the split normal modes in Fig. 2D of $\gamma_{\text{R}}=0.10$ GHz, which is the arithmetic average of γ_{FM} and γ_{QTA^*} as expected for their hybridization (see the Materials and Methods section for details).

A similar analysis for the QLA mode, for which the spatial distribution is demonstrated in the upper part of Fig. 4A, shows that the overlap of the FM mode with the optically excited QLA mode is nonzero ($\kappa_{\text{QLA}} \approx \beta_1$) and driving of the FM mode by the QLA mode should take place. This agrees with the experimental results in Fig. 3B where the increase of the KR signal in resonance is clearly seen. The absence of a normal mode splitting in this case could be related to the small value of κ_{QLA} , which can be estimated from analyzing the spectral widths of the interacting modes in and out of resonance [28]: $\kappa_{\text{QLA}}^2 = (\gamma_{\text{R}} - \gamma_{\text{QLA}})(\gamma_{\text{FM}} - \gamma_{\text{R}})$, where $\gamma_{\text{R}}=0.10$ GHz is the spectral width of the line at $f = f_{\text{FM}} = f_{\text{QLA}}$ as shown in Fig. 3A. (see the Materials and Methods section for details). We estimate $\gamma_{\text{QLA}}=0.03$ GHz like for the QTA mode and, thus, $\kappa_{\text{QLA}}=0.07$ GHz, which provides a cooperativity of $C_{\text{QLA}} \approx 1$. For such a “moderate coupling”, magnon polaron formation still can take place [8], but the avoided crossing is masked by the energy transfer from the phonon mode.

To demonstrate the difference between the two resonances and compare it with experiment, we consider a model of three coupled harmonic oscillators (the system of equations used for the calculations can be found in Materials and Methods). The result of this modeling is presented in Fig.

4B and shows the similarities with the experimental color map in Fig. 2, so that the model can be considered as appropriate for the involved physics. The main features of the magnon spectra in the calculated color map of Fig. 4B, i.e., the avoided crossing and the driving, are in good agreement with the experimentally measured spectra in Fig. 2A. Indeed, the avoided crossing is observed for the lower FM-QTA* resonance while for the upper FM-QLA resonance the splitting of the normal modes is masked by strong driving of the FM mode by resonant phonons.

Magnon polaron in the reflectivity signal

Strong magnon-phonon coupling and the formation of a magnon polaron can also be manifested in the field dependence of the transient reflectivity signal. The spectral amplitude of the QTA mode in $\Delta I(t)$ does not depend strongly on B , which agrees with our model where the lower QTA mode does not interact with the FM mode. In contrast, the contribution of the QLA mode to $\Delta I(t)$ demonstrates a strong dependence on B . Out of resonance the contribution of the QLA mode to the transient reflectivity is extremely weak, which is due to an inefficient photo-elastic effect (see Materials and Methods for details). The contribution increases significantly at the FM-QLA resonance for $B=140$ mT as demonstrated in the right panel of Fig. 3B and Fig. 3C. We attribute this increase to the QLA-FM interaction, which distorts the polarization of the phonon mode similarly to the case of bulk [29] and surface acoustic waves [30]. The in-plane shear component, η_{xy} , makes the QLA mode visible in the photo-elastic effect. In this case, the reflectivity signal, $\Delta I(t)$, for the QLA mode increases at the resonance field ($B=140$ mT), as observed in our experiment.

DISCUSSION

The direct observation of magnon polarons in the time domain demonstrated here paves the way for exploiting new degrees of freedom for spin excitation and the manipulation of spins and phonons at the nanoscale. Magnon polarons allow one to control spins via phonons and phonons via spins when no efficient direct excitation of these modes can be achieved by microwaves or optical techniques. This is explicitly demonstrated in our study, where we gain access to the QTA* phonon mode, while it cannot be excited optically. Moreover, the selectivity in coupling of the magnon and phonon modes allows us to isolate the resulting hybridized state from the optically active phonon mode of the same frequency. This selectivity, which is determined by the spatial overlap of the interacting modes, can be achieved also by alternative ways of spatial matching. For instance, one could imagine asymmetric periodic structures, the spatial profile of which provides efficient coupling of particular phonon and magnon modes, while other modes remain uncoupled.

The suggested approach is applicable for the manipulation of propagating magnon polarons. While the ability of surface acoustic waves to carry magnons across extremely long distances has been recently demonstrated in the weak coupling regime [31], the strong magnon-phonon coupling will enrich collective magnon-phonon transport by pronounced nonreciprocity and give access to the manipulation of the polarization of surface acoustic waves [30]. Another possibility is the localization of magnon polarons on a defect in a periodic structure due to the gap in the magnon spectrum. This is particularly important in the context of spin-spin interactions and the related phenomenon of magnon Bose-Einstein condensation [3]. An especially appealing prospect is to use the long coherence times and tunability of magnon polarons for creating states with well-defined magnon polaron numbers [32] or coherent magnon-photon-phonon states [33,34], thus providing new routes for quantum information and metrology.

MATERIALS AND METHODS

Sample growth and post-growth processing. A film of $\text{Fe}_{0.81}\text{Ga}_{0.19}$ of 105-nm thickness was epitaxially grown on a (001)-GaAs substrate on top of 10 periods of a GaAs/AlAs (59 nm/71 nm) superlattice. The Gallenol film was capped by a 3-nm thick Cr layer to prevent oxidation. The nanograting (NG) of $25 \times 25\text{-}\mu\text{m}^2$ size was fabricated by milling parallel grooves in the sample surface along the (100) crystallographic axis of the GaAs substrate using a focused beam of Ga ions (Raith VELION FIB-SEM). The grooves have a depth $a=7$ nm and a width $w=100$ nm, which equals their separation; the resulting NG lateral period is $d=200$ nm. The sample was fixed by silver paste to a massive copper plate which served as heat sink and was located between the poles of an electromagnetic coil.

Time-resolved pump-probe measurements. The pump-probe scheme was realized by two mode-locked Erbium-doped ring fiber lasers (TOPTICA FemtoFiber Ultra 1050 and FemtoFiber Ultra 780). The lasers generate pulses of 150-fs duration with a repetition rate of 80 MHz at wavelengths of 1046 nm (pump pulses) and 780 nm (probe pulses). The energy density in the focused pump spot of 5- μm diameter was 12 mJ/cm². The energy density in the 1- μm -diameter spot of the linearly polarized probe pulse at the NG surface was 1 mJ/cm². Detection of the Kerr rotation of the probe pulse's polarization plane was obtained in a differential scheme, based on a Wollaston prism and a balanced optical receiver with 10-MHz bandwidth. The modulation of the probe pulse intensity was measured by a single photodiode with no polarization optics in the optical path of the probe beam after reflection from the sample. Temporal resolution was achieved by asynchronous optical sampling (ASOPS) [35]. The pump and probe oscillators were locked with a frequency offset of 800 Hz. In combination with the 80-MHz repetition rate, this allows measurement of the time-resolved signals in a time window of 12.5 ns with a time resolution limited by the probe pulse duration. The main measurements were carried out in the geometry with excitation of the NG by the pump pulses through the GaAs substrate, which is transparent at the pump wavelength. The measurements for characterizing the phonon and magnon modes were performed at the NG front-side. The reflectivity signal in Fig. 1C was measured at $B=250$ mT, applied along the NG grooves when the phonon and magnon modes are fully uncoupled [22].

Analysis of the transient signals. For obtaining the main parameters of the magnon and phonon modes as well as of their hybridized state, the transient reflectivity and Kerr rotation signals were analyzed by fast Fourier transformation (FFT) and fitting. For the FFT analysis we used rectangular envelope windows with a width of 10 ns. This allowed us to obtain the frequencies and spectral widths of the main harmonics contributing to the transient signal with a resolution of 0.1 GHz. For fitting the transient signals we used the following function: $y(t) = \sum A_j e^{-t/\tau_j} \sin(2\pi f_j t - \varphi_j)$, where A_j , τ_j , f_j , and φ_j are the amplitude, lifetime, frequency and phase of the j^{th} harmonic contributing to the measured transient signal. Summation of three harmonics was enough for fitting any experimental signal with high accuracy. The spectral power density of this function obtained by Fourier transformation consists of Lorentzian peaks centered at f_j with spectral width (HWHM) $\gamma_j = 1/2\pi\tau_j$. The estimated errors of f_j and γ_j are ± 0.002 GHz and ± 0.02 GHz, respectively.

Modeling the NG phonon modes (spectral and spatial distribution, excitation and detection). The coherent elastic response of the NG and its optical detection were modeled using finite element methods in the COMSOL Multiphysics® software (version 5.4) [36]. The spatial distributions of the strain components and the frequencies of the NG modes were obtained by solving the elasticity equations within the eigenmode problem [17,27]. The optical excitation and detection of the NG phonon modes were modeled in the time domain by solving the Maxwell equations and the system of elasticity equations in which the optically generated thermal stress obtained within the two-temperature model [15] was considered as a time- and spatially dependent driving force. The FFT spectra of the calculated optically excited dynamical strain and corresponding transient reflectivity signal as well as the material parameters used for the calculations [37-40] are presented in the Supplementary Material.

Modeling the interaction of three harmonic oscillators. The interaction of the phonon and magnon modes in the NG is described by a model of three interacting oscillators using the following system of equations:

$$\frac{1}{2\pi} \frac{da_j}{dt} + \gamma_j a_j + i f_j a_j - i \sum_l K_{jl} a_l = A_j \delta(t), \quad (3)$$

where a_j are the complex amplitudes ($j=QTA^*$, QLA, or FM). The coupling tensor \hat{K} has the form

$$\hat{K} = \begin{pmatrix} 0 & 0 & \kappa_{QTA^*} \\ 0 & 0 & \kappa_{QLA} \\ \kappa_{QTA^*} & \kappa_{QLA} & 0 \end{pmatrix}, \quad (4)$$

where κ_{QTA^*} and κ_{QLA} are the coupling strengths of the respective phonon mode and the FM mode. Figure 4B in the main text shows the FFT (spectral density) of $a_{FM}(t)$ obtained by the analytical solution for the following parameters: $A_{QTA^*} = 0$, $A_{QLA} = 10$, $A_{FM} = 1$, $f_{QTA^*} = 13.0$ GHz, $f_{QLA} = 14.6$ GHz, $f_{FM} = 7.12 + \alpha B$ GHz, where $\alpha = 53$ GHz·T⁻¹; $\gamma_{QTA^*} = \gamma_{QLA} = 0.03$ GHz, $\gamma_{FM} = 0.17$ GHz; $\kappa_{QTA^*} = 0.20$ GHz; $\kappa_{QLA} = 0.07$ GHz. The relation A_{QLA}/A_{FM} corresponds to the amplitudes and corresponding energies of the QLA phonon mode and the magnetization precession excited by the pump pulse. At the resonance of the magnon mode with the phonon modes the solutions for the resonance frequency read:

$$f_{R,n} = f_n - i \frac{\gamma_{FM} + \gamma_n}{2} \pm \sqrt{\kappa_n^2 - \left(\frac{\gamma_{FM} - \gamma_n}{2} \right)^2}, \quad (5)$$

where n stands for QTA* or QLA, f_n is the frequency of the uncoupled QTA* or QLA modes. The real and imaginary part of $f_{R,n}$ gives the frequency and damping of the corresponding magnon-phonon wave. In the case of strong coupling, when $\kappa_n \geq \left| \frac{\gamma_{FM} - \gamma_n}{2} \right|$, the damping of two hybridized split resonances is given by $\frac{\gamma_{FM} + \gamma_n}{2}$. In the case of weak (or moderate) coupling, $\kappa_n < \left| \frac{\gamma_{FM} - \gamma_n}{2} \right|$, and the damping, γ_R , reads

$$\gamma_R = \frac{\gamma_{FM} + \gamma_n}{2} \mp \sqrt{\left(\frac{\gamma_{FM} - \gamma_n}{2} \right)^2 - \kappa_n^2}. \quad (6)$$

REFERENCES AND NOTES

- [1] M. Weiler, H. Huebl, F. S. Goerg, F. D. Czeschka, R. Gross, S. T. B. Goennenwein, Spin pumping with coherent elastic waves. *Phys. Rev. Lett.* **108**, 176601 (2012).
- [2] T. Kikkawa, K. Shen, B. Flebus, R. A. Duine, K. Uchida, Z. Qiu, G. E. W. Bauer, E. Saitoh, Magnon polarons in the spin Seebeck Effect. *Phys. Rev. Lett.* **117**, 207203 (2016).
- [3] D. A. Bozhko, P. Clausen, G. A. Melkov, V. S. L'vov, A. Pomyalov, V. I. Vasyuchka, A. V. Chumak, B. Hillebrands, A. A. Serga, Bottleneck accumulation of hybrid magnetoelastic bosons. *Phys. Rev. Lett.* **118**, 237201 (2017).
- [4] L. J. Cornelissen, K. Oyanagi, T. Kikkawa, Z. Qiu, T. Kuschel, G. E. W. Bauer, B. J. van Wees, and E. Saitoh, Nonlocal magnon-polaron transport in yttrium iron garnet. *Phys. Rev. B* **96**, 104441 (2017).
- [5] J. Holanda, D. S. Maior, A. Azevedo, S. M. Rezende, Detecting the phonon spin in magnon-phonon conversion experiments. *Nature Physics* **14**, 500–506 (2018).
- [6] H. Hayashi, K. Ando, Spin pumping driven by magnon polarons. *Phys. Rev. Lett.* **121**, 237202 (2018).
- [7] C. Berk, M. Jaris, W. Yang, S. Dhuey, S. Cabrini, H. Schmidt, Strongly coupled magnon-phonon dynamics in a single nanomagnet. *Nat. Commun.* **10**, 2652 (2019).
- [8] C. Kittel, Interaction of spin waves and ultrasonic waves in ferromagnetic crystals. *Phys. Rev.* **110**, 836-841 (1958).
- [9] A. I. Akhiezer, V. G. Bar'iakhtar, S. V. Peletminskii, Coupled magnetoelastic waves in ferromagnetic media and ferroacoustic resonance. *Sov. Phys. JETP* **35**, 157 -164 (1959).
- [10] O. Yu. Belyaeva, S. N. Karpachev, L. K. Zarembo, Magnetoacoustics of ferrites and magnetoacoustic resonance. *Sov. Phys. Uspekhi* **35**, 106-122 (1992) and the references therein.
- [11] S. R.-K. Rodriguez, Classical and quantum distinctions between weak and strong coupling. *Eur. J. Phys.* **37**, 025802 (2016).
- [12] J. Atulasimha, A. B. Flatau, A review of magnetostrictive iron-gallium alloys. *Smart Mater. Struct.* **20**, 043001 (2011).
- [13] D. E. Parkes, L. R. Shelford, P. Wadley, V. Holý, M. Wang, A. T. Hindmarch, G. van der Laan, R. P. Campion, K. W. Edmonds, S. A. Cavill, A. W. Rushforth, Magnetostrictive thin films for microwave spintronics, *Sci. Reports* **3**, 2220 (2013).
- [14] A. V. Scherbakov, A. P. Danilov, F. Godejohann, T.L. Linnik, B.A. Glavin, L.A. Shelukhin, D.P. Pattnaik, M. Wang, A.W. Rushforth, D.R. Yakovlev, A.V. Akimov, M. Bayer, Optical excitation of single- and multimode magnetization precession in Fe-Ga nanolayers. *Phys. Rev. Applied* **11**, 031003 (2019).
- [15] C. Thomsen, H. T. Grahn, H. J. Maris, J. Tauc, Surface generation and detection of phonons by picosecond light pulses. *Phys. Rev. B* **34**, 4129-4138 (1986).
- [16] W. K. Hiebert, A. Stankiewicz, M. R. Freeman, Direct observation of magnetic relaxation in a small permalloy disk by time-resolved scanning Kerr microscopy, *Phys. Rev. Lett.* **79**, 1134 (1997).
- [17] D. Nardi, M. Travaglini, M. E. Siemens, Q. Li, M. M. Murnane, H. C. Kapteyn, G. Ferrini, F. Parmigiani, F. Banfi, Probing thermomechanics at the nanoscale: Impulsively excited pseudosurface acoustic waves in hypersonic phononic crystals. *Nano Lett.* **11**, 4126–4133 (2011).

- [18] J. Janušonis, C. L. Chang, P. H. M. van Loosdrecht, R. I. Tobey, Frequency tunable surface magneto elastic waves. *Appl. Phys. Lett.* **106**, 181601 (2015).
- [19] M. Langer, R. A. Gallardo, T. Schneider, S. Stienen, A. Roldán-Molina, Y. Yuan, K. Lenz, J. Lindner, P. Landeros, J. Fassbender, Spin-wave modes in transition from a thin film to a full magnonic crystal. *Phys. Rev. B* **99**, 024426 (2019).
- [20] M. van Kampen, C. Jozsa, J. T. Kohlhepp, P. LeClair, L. Lagae, W. J. M. de Jonge, B. Koopmans, All-optical probe of coherent spin waves, *Phys. Rev. Lett.* **88**, 227201 (2002).
- [21] V. N. Kats, T. L. Linnik, A. S. Salasyuk, A. W. Rushforth, M. Wang, P. Wadley, A. V. Akimov, S. A. Cavill, V. Holy, A. M. Kalashnikova, A. V. Scherbakov, Ultrafast changes of magnetic anisotropy driven by laser-generated coherent and noncoherent phonons in metallic films. *Phys. Rev. B* **93**, 214422 (2016).
- [22] A. S. Salasyuk, A. V. Rudkovskaya, A. P. Danilov, B. A. Glavin, S. M. Kukhtaruk, M. Wang, A. W. Rushforth, P. A. Nekludova, S. V. Sokolov, A. A. Elistratov, D. R. Yakovlev, M. Bayer, A. V. Akimov, A. V. Scherbakov, Generation of a localized microwave magnetic field by coherent phonons in a ferromagnetic nanograting. *Phys. Rev. B* **97**, 060404(R) (2018).
- [23] M. Weiler, L. Dreher, C. Heeg, H. Huebl, R. Gross, M. S. Brandt, and S. T. B. Goennenwein, Elastically driven ferromagnetic resonance in nickel thin films. *Phys. Rev. Lett.* **106**, 117601 (2011).
- [24] Y. Yahagi, B. Harteneck, S. Cabrini, H. Schmidt, Controlling nanomagnet magnetization dynamics via magnetoelastic coupling. *Phys. Rev. B* **90**, 140405(R) (2014).
- [25] J. V. Jäger, A. V. Scherbakov, B. A. Glavin, A. S. Salasyuk, R. P. Champion, A. W. Rushforth, D. R. Yakovlev, A. V. Akimov, M. Bayer, Resonant driving of magnetization precession in a ferromagnetic layer by coherent monochromatic phonons. *Phys. Rev. B* **92**, 020404(R) (2015).
- [26] R. Verba, I. Lisenkov, I. Krivorotov, V. Tiberkevich, and A. Slavin, Nonreciprocal surface acoustic waves in multilayers with magnetoelastic and interfacial Dzyaloshinskii-Moriya interactions. *Phys. Rev. Applied* **9**, 064014 (2018).
- [27] J. Sadhu, J. H. Lee, S. Sinha, Frequency shift and attenuation of hypersonic surface acoustic phonons under metallic gratings. *Appl. Phys. Lett.* **97**, 133106 (2010).
- [28] P. F. Herskind, A. Dantan, J. P. Marler, M. Albert, M. Drewsen, Realization of collective strong coupling with ion Coulomb crystals in an optical cavity. *Nature Phys.* **5**, 494-498 (2009).
- [29] H. Matthews, R. C. LeCraw Acoustic wave rotation by magnon-phonon interaction. *Phys. Rev. Lett.* **8**, 397-399 (1962).
- [30] R. Q. Scott, D. L. Mills, Propagation of surface magnetoelastic waves on ferromagnetic crystal substrates. *Phys. Rev. B* **15**, 3545-3557 (1977).
- [31] B. Casals, N. Statuto, M. Foerster, A. Hernández-Mínguez, R. Cichelero, P. Manshausen, A. Mandziak, L. Aballe, J. M. Hernández, F. Macià, Generation and imaging of magnetoacoustic waves over millimeter distances. *Phys. Rev. Lett.* **124**, 137202 (2020).
- [32] Y. Chu, P. Kharel, T. Yoon, L. Frunzio, P. T. Rakich, R. J. Schoelkopf, Creation and control of multi-phonon Fock states in a bulk acoustic-wave resonator. *Nature* **563**, 666 (2018).
- [33] X. Zhang, C.-L. Zou, L. Jiang, H. X. Tang, Cavity Magnomechanics, *Sci. Adv.* **2**, e1501286 (2016).
- [34] J. Li, S.-Y. Zhu, G. S. Agarwal, Magnon-photon-phonon entanglement in cavity magnomechanics. *Phys. Rev. Lett.* **121**, 203601 (2018).
- [35] A. Bartelsa, R. Cerna, C. Kistner, A. Thoma, F. Hudert, C. Janke, and T. Dekorsy, Ultrafast time-domain spectroscopy based on high-speed asynchronous optical sampling. *Rev. Sci. Instrum.* **78**, 035107 (2007).

- [36] COMSOL Multiphysics® v. 5.4. <http://www.comsol.com>. COMSOL AB, Stockholm, Sweden.
- [37] A. E. Clark, K. B. Hathaway, M. Wun-Fogle, J. B. Restorff, T. A. Lograsso, V. M. Keppens, G. Petculescu, R. A. Taylor, Extraordinary magnetoelasticity and lattice softening in bcc Fe-Ga alloys. *J. Appl. Phys.* **93**, 8621–8623 (2003).
- [38] O. Madelung, *Semiconductors: Data Handbook* (Springer, 2004).
- [39] M. A. Ordal, R. J. Bell, R. W. Alexander, L. A. Newquist, M. R. Query, Optical properties of Al, Fe, Ti, Ta, W, and Mo at submillimeter wavelengths. *Appl. Opt.* **27**, 1203-1209 (1988).
- [40] T. Skauli, P. S. Kuo, K. L. Vodopyanov, T. J. Pinguet, O. Levi, L. A. Eyres, J. S. Harris, M. M. Fejer, B. Gerard, L. Becouarn, E. Lallier, Improved dispersion relations for GaAs and applications to nonlinear optics. *J. Appl. Phys.* **94**, 6447–6455 (2003).

Acknowledgements: We acknowledge Boris Glavin (†) for his valuable contribution to this work. We are thankful to Mikhail Glazov, Tetiana Linnik and Vitaly Gusev for fruitful discussions.

Funding: The work was supported by the Bundesministerium für Bildung und Forschung through the project VIP+ "Nanomagneton" and by the Deutsche Forschungsgemeinschaft and the Russian Foundation for Basic Research (Grants No. 19-52-12065 and 19-52-12038) in the frame of the International Collaborative Research Center TRR 160. The growth and characterization of the Galfenol-based nanostructures were supported by the Engineering and Physical Sciences Research Council (grant number: EP/H003487/1). A.N.P. acknowledges the partial financial support of the Russian President Grant No. MD-5791.2018.2.

Author contributions: F.G. constructed the experimental setup, carried out the experiment and performed the data analysis. A.V.S. and A.V.A. designed the experiment and supervised the experiment and theoretical modeling, S.M.K. designed the nanogratings and performed the theoretical analysis and numerical modeling, A.N.P. discussed and modeled the experimental data, D.D.Y. performed the experiment and characterized the nanograting by atomic force microscopy, M. W. deposited the Galfenol films, A. N. produced the nanogratings, A.W.R. designed the Galfenol samples and performed the numerical modeling, A.V.S., A.V.A., F.G., S.M.K., A.W.R., D.R.Y., and M.B. discussed the results and wrote the manuscript.

Competing interests: The authors declare no competing interests.

Data availability: The data that support the plots within this paper and other findings of this study are available from the corresponding authors upon reasonable request. HIM

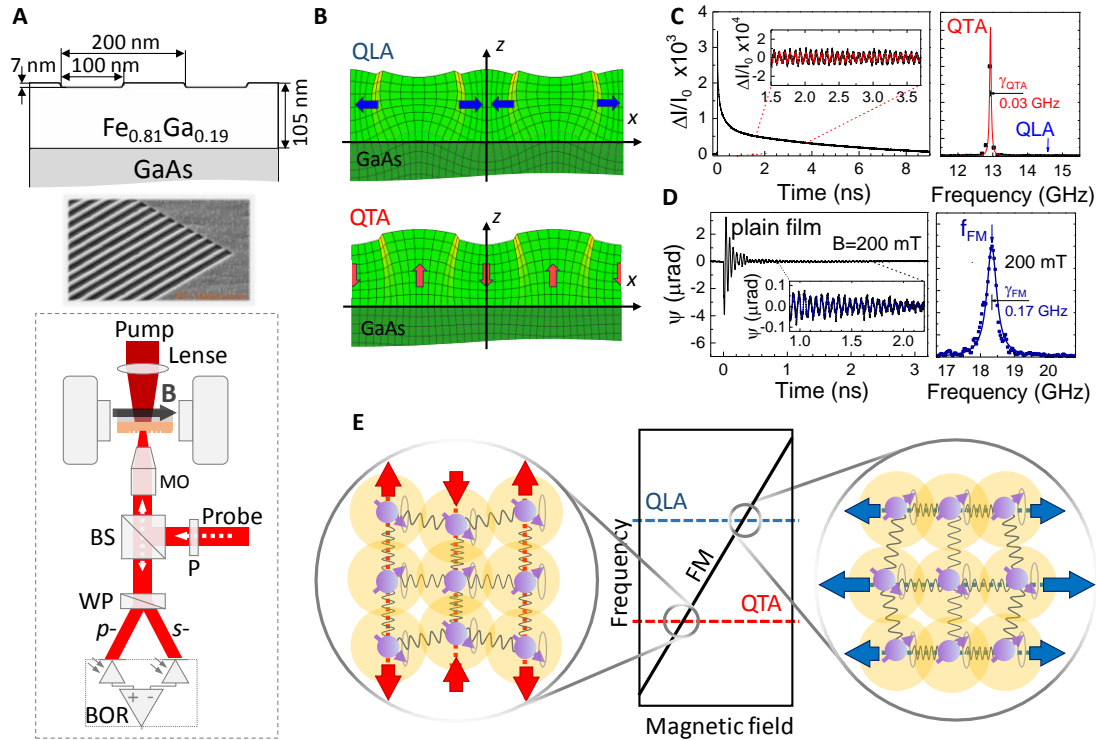


Fig 1. Phonons and magnons in a Galfenol nanograting. (A) Design and SEM image of the studied sample, as well as the experimental setup: MO – microscope objective, WP – Wollaston prism, BOR – balanced optical receiver, BS – beam splitter, P - polarizer. (B) Calculated displacements for two phonon modes excited by the pump pulse. Black arrows illustrate the used coordinate system. The blue and red arrows indicate the main lattice motions for the two modes. (C) Transient reflectivity signal and its fast Fourier transform (FFT) recorded on the grating. The inset shows a close-up of the transient signal after subtraction of the slow background. (D) Transient Kerr rotation (KR) signal measured from an unpatterned part of the studied film and its FFT taken for $t > 1$ ns. The inset shows a zoomed fragment of the transient KR signal, when the fundamental magnon mode solely contributes to the magnetization precession. In both panels ((C) and (D)) the experimental transients in the insets and their FFTs are shown by symbols, while the fits and their FFTs are shown by solid lines. (E) Diagram demonstrating the idea of the experiment: the field-dependent magnon mode (oblique line) can be tuned into resonance with the field-independent phonon modes (horizontal lines) by an external magnetic field. The crossing points correspond to the FM-QTA and FM-QLA resonances where magnon-phonon hybridization is expected.

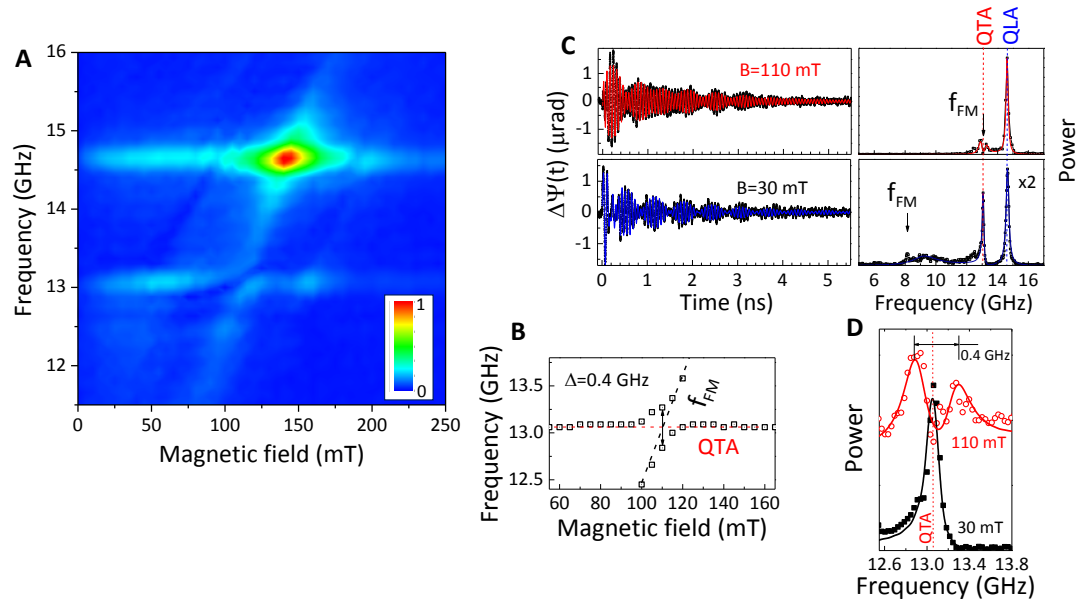


Fig. 2. Hybridization of magnon and phonon modes. (A) Color map showing the spectral density of the measured KR signal as function of the external magnetic field. The anti-crossing is observed at $f=13$ GHz and $B=110$ mT. (B) Magnetic field dependence of the peak frequencies in the magnon spectrum around the intersection of the QTA and FM modes. (C) KR signals (left panels) and their FFTs (right panels) at non-resonant ($B=30$ mT) and resonant ($B=110$ mT) conditions. Symbols show the measured signals and their FFTs; solid lines show corresponding fits and their FFTs. (D) Zoomed fragments of the FFT spectra shown in (C) around the resonance frequency. The normal mode splitting for the resonance at $B=110$ mT is clearly seen.

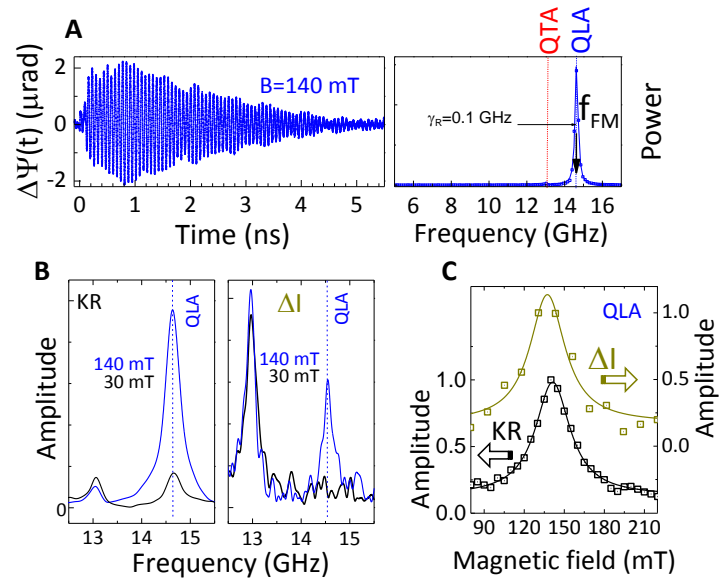


Fig. 3. Phonon driving of magnons.

(A) Kerr rotation signal and its FFT measured at $B=140\text{ mT}$, corresponding to the resonance of the FM and QLA phonon modes. (B) FFTs around f_{QLA} obtained from the KR (left panel) and reflectivity (right panel) signals measured for resonant ($B=140\text{ mT}$) and non-resonant ($B=30\text{ mT}$) conditions. (C) Magnetic field dependences of the normalized amplitudes at $f=f_{\text{QLA}}=14.5\text{ GHz}$ for the Kerr rotation (lower) and reflectivity (upper) signals (lines are guides to the eye).

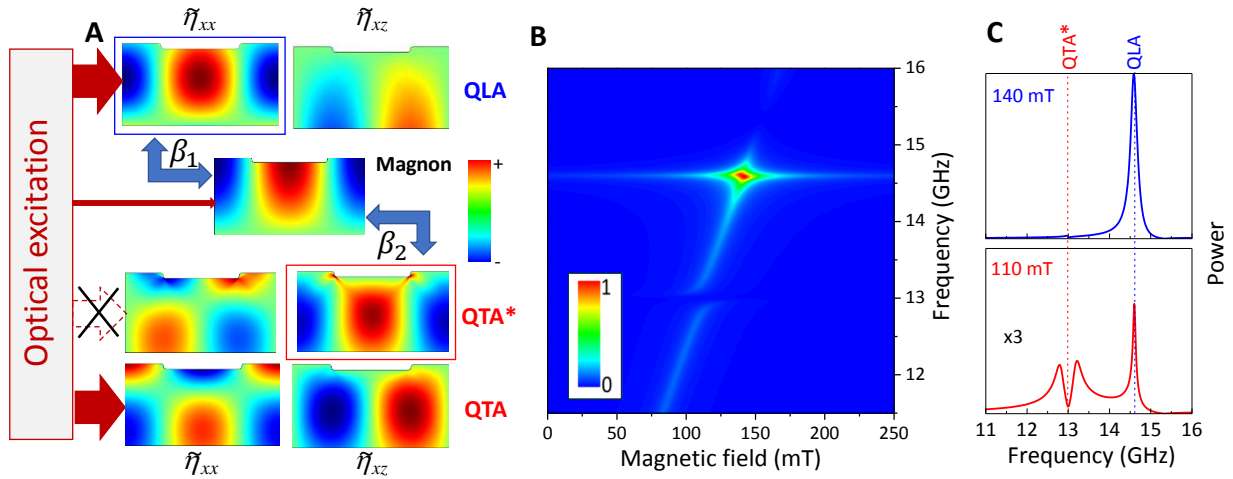


Fig. 4. Modeling of magnon polaron formation and spectrum. (A) Spatial distributions of the normalized dynamic magnetization of the fundamental magnon mode and the normalized strain components for the symmetric QTA, antisymmetric QTA* and symmetric QLA modes. The blue arrows indicate the mode pairs, for which the overlap integrals have non-negligible values. (B) The color map shows the calculated magnetic field dependence of the spectral density of the magnon states calculated in the model of three coupled harmonic oscillators. The initial conditions for the calculations are set as following: the lower QTA* mode is not excited (as mentioned in the text), the energy transfer from the pump pulse to the upper QLA mode significantly exceeds the energy transferred to the FM mode. (C) Calculated magnon spectral power density for magnetic fields corresponding to the resonances of the FM mode with the QTA* mode ($B=110$ mT) and the QLA mode ($B=140$ mT).

SUPPLEMENTARY MATERIALS

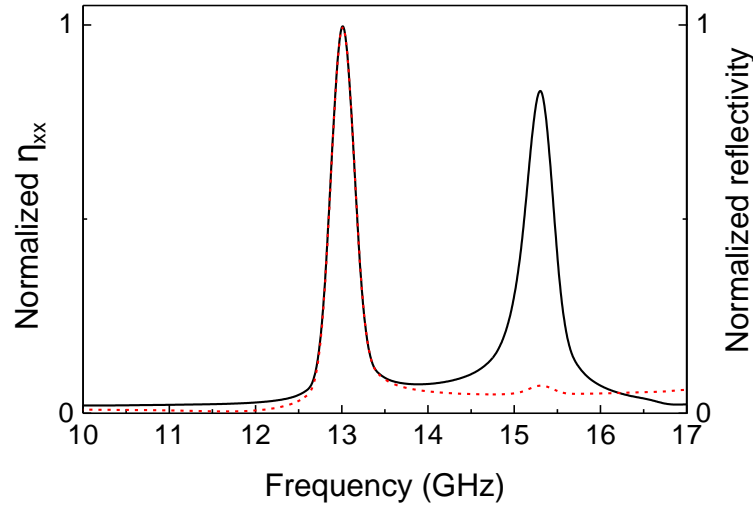


Fig. S1. Normalized FFT spectra of the calculated dynamical strain excited in the studied nanograting by the pump pulse (black line) and the corresponding transient reflectivity signal, $\Delta I(t)$ (red line). Amplitudes of the optically excited QTA and QLA phonon modes are almost equal, but the contribution of the QLA mode to the transient reflectivity signal is negligible in agreement with the experimental observation. The material parameters used for calculations are summarized in Table S1.

Table S1. Material parameters used for numerical modeling

Acoustic parameters					
	c_{11} , GPa	c_{12} , GPa	c_{44} , GPa	ρ , kg/m ³	Ref.
$Fe_{0.81}Ga_{0.1}$	209*	141*	113*	7800	(37)
$GaAs$	119	53.8	59.5	5316	(38)
$AlAs$	119.9	57.5	56.6	3760	(38)
Optical parameters: pump light					
λ_{pump} , nm	n_{GaAs}	n_{FeGa}			Citation
1046	3.4805	$3.2196 + i \cdot 4.2740$			(39,40)
Optical parameters: probe light					
λ_{probe} , nm	n_{GaAs}	n_{FeGa}	$-n_{FeGa}^2 p_{11}$	$-n_{FeGa}^2 p_{12}$	Citation
760	$3.7137 + i \cdot 0.097862$	$2.9688 + i \cdot 3.5337$	1**	$1.1 - i \cdot 1.1$ **	(39,40)

*parameters were slightly adjusted for better describing the experiment ($\approx 10\%$).

**parameters were obtained by fitting the experimental data

Notations used in Table S1:

c_{ij} are the stiffness matrix elements, ρ is the mass density; λ_{pump} and λ_{probe} are the wavelengths of the pump and probe pulses, n_{GaAs} and n_{FeGa} are the respective refractive indexes, p_{11} and p_{12} are the photo-elastic coefficients.